Alloying of gold with palladium: An effective strategy to improve catalytic stability and chlorine-tolerance of the 3DOM CeO$_2$-supported catalysts in trichloroethylene combustion

Xing Zhang, Yuxi Liu[*], Jiguang Deng, Xiaohui Yu, Zhuo Han, Kunfeng Zhang, Hongxing Dai[*]

Beijing Key Laboratory for Green Catalysis and Separation, Key Laboratory of Beijing on Regional Air Pollution Control, Key Laboratory of Advanced Functional Materials, Education Ministry of China, Laboratory of Catalysis Chemistry and Nanoscience, Department of Chemistry and Chemical Engineering, College of Environmental and Energy Engineering, Beijing University of Technology, Beijing, 100124, China

ABSTRACT

The three-dimensionally ordered macroporous (3DOM) CeO$_2$-supported Au–Pd alloys (xAuPd$_y$/3DOM CeO$_2$, x is the total loading (wt%) of Au and Pd, and y is the Pd/Au molar ratio) were synthesized using the polymethyl methacrylate-templating and polyvinyl alcohol-protected reduction methods. The samples were characterized by a number of analytical techniques, and their catalytic performance was evaluated for the combustion of trichloroethylene (TCE). It is found that the xAuPd$_y$/3DOM CeO$_2$ samples displayed a good-quality 3DOM architecture, and the noble metal nanoparticles (NPs) with a size of 3–4 nm were uniformly dispersed on the skeleton surface of 3DOM CeO$_2$. Among all of the samples, 2.85AuPd$_{1.87}$/3DOM CeO$_2$ exhibited the highest catalytic activity, with the temperature at a TCE conversion of 90% ($T_{90\%}$) being 415 °C at a space velocity of 20,000 mL/(g h). Furthermore, the 2.85AuPd$_{1.87}$/3DOM CeO$_2$ sample possessed the lowest apparent activation energy (33 kJ/mol), excellent catalytic stability, and good moisture- and chlorine-tolerant behaviors. Alloying of Au with Pd changed the pathway of TCE oxidation and reduced formation of perchloroethylene. We conclude that the excellent catalytic performance for TCE combustion of 2.85AuPd$_{1.87}$/3DOM CeO$_2$ was associated with the highly dispersed AuPd$_{1.87}$ alloy NPs, high adsorbed oxygen species concentration, good low-temperature reducibility, and strong interaction between AuPd$_{1.87}$ NPs and 3DOM CeO$_2$ as well as the high-quality 3DOM structure and high surface acidity.

1. Introduction

Chlorinated volatile organic compounds (CVOCs) as an irreplaceable solvent are widely used in industries. Such compounds are often of an environmentally persistent nature and their emissions can induce toxic effects on human health and wildlife [1,2]. Therefore, an efficient method to remove the CVOCs is urgently needed. Among the CVOCs abatement methods developed so far, catalytic combustion is promising since it operates at low temperatures and can convert CVOCs into harmless compounds. Ideal catalytic combustion of CVOCs is merely formation of carbon dioxide, water, and hydrogen chloride, and the key issue of such a technology is the availability of high-performance catalysts. Up to now, supported noble metal and (mixed) transition-metal oxide catalysts have been developed. Over the transition-metal oxide catalysts, however, formation of volatile metal oxychlorides, coke, and intermediate byproducts could lead to loss of the active phases, deactivation in catalytic activity, and generation in refractory organics [3].

Supported noble metal catalysts showed excellent activity, high selectivity, and good resistance against volatilization [4], so it becomes the most promising catalyst to remove VOCs. For instance, Chen et al. [5] observed that Pt supported on Al$_2$O$_3$−CeO$_2$ was highly active and stable for the oxidation of dichloromethane. Xie et al. [6] designed a novel approach by introducing a certain amount of CoO to the supported Au−Pd alloy NPs to prepare high-performance Au−Pd−xCoO/3DOM Co$_3$O$_4$ catalysts, and found that Au–Pd–0.40CoO/3DOM Co$_3$O$_4$ performed the best with the temperature ($T_{90\%}$) at a methane conversion of 90% being 341 °C at a space velocity of 20 000 mL/(g h). Recently, Wang and coworkers [7] have prepared the bimetallic Au−Pd alloy NPs dispersed on the surface of 3DOM La$_{0.6}$Sr$_{0.4}$MnO$_3$ (LSMO) and claimed that formation of the Au−Pd alloy NPs favored the enhancement in catalytic activity for methane combustion since the 3DOM LSMO support possessed a large surface area (beneficial for high dispersion of the noble metal NPs), abundant Brønsted acid sites (facilitating adsorption and activation of the

---

reactants), and thermal stability. An and coworkers [2] investigated the PtCu/CeO$_2$ catalysts for the instant mineralization of paraffinic VOCs under photothermocatalytic conditions, and observed that low loadings of Pt–Cu alloy clusters on the CeO$_2$ surface led to improved charge separation, increased generation of reactive oxygen species, and promoted dynamic balance of Cu$^+$/Cu^0 or Cu^{2+}/Cu^0 with high photothermocatalytic stability. In addition, the same group also found that the foam nickel-supported MO$_x$–TiO$_2$ (MO$_x$/TiFN; M = Cu, Mn, Ag) catalysts showed good performance in the photocatalytic ozonation of gaseous alkanes [8,9].

CeO$_2$, one of the most active rare earth oxides, has attracted much attention owing to its unique physicochemical properties (e.g., ample oxygen vacancies and excellent Ce^{3+}/Ce^{4+} redox ability) in the past few decades. Some researchers found that the ceria-based catalysts were highly selective and anti-poisoning for the oxidative removal of CVOCs in a wide temperature range [10,11]. Structural property of a catalyst is important in catalyzing the surface reactions, especially at high space velocity. Three-dimensionally ordered macropores structures are beneficial for enhancing mass transfer of the VOC molecules and effectively dispersing the active sites on the skeleton surface, thus the catalytic activity and selectivity of trichloroethylene combustion were improved [12]. Catalytic activity of a 3DOM metal oxide is usually low due to its unsatisfactory ability of O$_2$ adsorption and activation. In order to increase the active oxygen species and the amount of active sites, we can load noble metal NPs on the surface of a 3DOM metal oxide to strengthen adsorption and activation of the reactants (i.e., O$_2$ and CVOCs) by forming oxygen vacancies or coordinatively unsaturated metal sites at the interface between noble metal NPs and metal oxide support [7]. Up to now, there was no reported that using 3DOM CeO$_2$ as support and AuPd alloys as active component to generate the AuPd/3DOM CeO$_2$ catalysts for the combustion of CVOCs in the literature.

We have previously investigated the preparation and characterization of AuPd/3DOM Co$_3$O$_4$ [13] and AuPd/3DOM La$_{0.6}$Sr$_{0.4}$MnO$_3$ [7] and their catalytic performance. We found that most of them performed well for the combustion of the typical VOCs. In this work, we adopted the polymethyl methacrylate (PMMA)-templating and polyvinyl alcohol (PVA)-protected reduction methods to prepare the xAuPd$_y$/3DOM CeO$_2$ catalysts, characterized physicochemical properties of the materials, and evaluated their activities for TCE combustion. In addition, we also examined catalytic stability of the typical catalyst in the presence of moisture, carbon dioxide or hydrogen chloride.

2. Experimental

2.1. Catalyst preparation

Li et al. [14] described a method for synthesizing well-arrayed colloidal crystal PMMA microspheres with an average diameter of ca. 300 nm (Fig. S1). 3DOM-structured CeO$_2$ with mesoporous walls were fabricated using the surfactant-assisted PMMA-templating strategy (Scheme S1) [15]. The 3DOM CeO$_2$-supported AuPd alloy NPs (xAuPd$_y$/3DOM CeO$_2$; x was the total loading (wt%) of Au and Pd, and y was the Pd/Au molar ratio)) were prepared via a PVA-protected reduction route using polyvinyl alcohol (PVA, MW = 10,000 g/mol) as the protecting agent and NaBH$_4$ as the reducing agent. The preparation process (Scheme S2) can be seen from the Supplementary material. By using the ICP–AES technique, the actual AuPd$_y$ loading (x) in xAuPd$_y$/3DOM CeO$_2$ was 0.46, 0.93, 1.41, and 2.85 wt%, and the actual Pd/Au molar ratio (y) in the samples was 1.92, 1.89, 1.82, and 1.87 (Table 1), respectively. In addition, the actual Au and Pd loadings in xAu/3DOM TiO$_2$ and xPd/3DOM TiO$_2$ was 0.91 and 0.86 wt%, respectively.

2.2. Catalyst characterization

All of the catalysts were characterized by means of a number of techniques, such as ICP–AES, X-ray diffraction (XRD), laser Raman

Table 1
Actual noble metal contents, CeO$_2$ crystallite sizes (D), noble metal particle sizes, macro- and mesopore diameters, BET surface areas, and pore volumes of the as-prepared samples.

Sample	Actual Au content[a] (wt%)	Actual Pd content[a] wt%	Actual Pd/Au molar ratio[a] (mol/mol)	D[b] (nm)	Noble metal particle size[c] (nm)	Macropore diameter[d] (nm)	Mesopore diameter[e] (nm)	BET surface area[e] (m²/g)	Pore volume[e] (cm³/g)
3DOM CeO$_2$	–	–	–	46	–	160–190	3.0–4.1	42.3	0.206
0.91Au/3DOM CeO$_2$	0.91	–	–	45	3.2	175–190	2.5–4.0	37.2	0.201
0.86Pd/3DOM CeO$_2$	–	0.86	–	49	3.1	165–185	2.6–4.1	37.7	0.205
0.46AuPd$_{1.85}$/3DOM CeO$_2$	0.23	0.23	1.85	47	2.9	160–185	2.7–4.2	37.3	0.210
0.93AuPd$_{1.89}$/3DOM CeO$_2$	0.46	0.47	1.89	46	3.2	165–190	2.6–4.0	36.9	0.204
1.41AuPd$_{1.82}$/3DOM CeO$_2$	0.50	0.91	1.82	47	3.5	165–185	2.4–4.1	37.1	0.203
2.85AuPd$_{1.87}$/3DOM CeO$_2$	1.42	1.43	1.87	48	3.3	160–190	2.8–4.3	35.6	0.207

[a] Data were determined by the ICP–AES technique.
[b] Data were estimated according to the Scherrer equation using the FWHM of the (101) line of CeO$_2$.
[c] Data were estimated according to the HRTEM images of the noble metal NPs on the surface of the samples.
[d] Data were estimated according to the SEM images.
[e] Data were determined by the BET method.

spectroscopy (Raman), scanning electron microscopy (SEM), high-resolution transmission electron microscopy (HRTEM), high angle annular dark field–scanning transmission electron microscopy (HAADF–STEM), N_2 adsorption–desorption (BET), X-ray photoelectron spectroscopy (XPS), temperature-programmed reduction (TPR), temperature-programmed desorption (TPD), temperature-programmed surface reaction (TPSR), and in-situ diffuse reflectance infrared Fourier transform spectroscopy (DRIFTS). The detailed characterization procedures were provided in the Supplementary material.

2.3. Catalytic activity evaluation

We measured catalytic activities of the samples in a continuous flow fixed-bed quartz microreactor (i.d. = 6 mm). 50 mg of the sample (40–60 mesh) was mixed with 0.25 g of quartz sand (40–60 mesh) for minimization of hot spots. The reactant feed was 750 ppm TCE + 20 vol % O_2 + N_2 (balance) with a total flow of 16.7 mL/min, and the space velocity (SV) was ca. 20,000 mL/(g h). We used the Agilent GC(5977A MSD)–MS(7890B) equipment to online detect the possible intermediates and products. 3.0 and 5.0 vol% H_2O were introduced to the reaction system using a water saturator at 23 and 34 °C, respectively. In the case of HCl addition, 100 ppm HCl from a gas cylinder with N_2 as balance was added to the reaction system. To examine the effect of CO_2 on catalytic activity of the typical sample, 3.0 or 7.0 vol% CO_2 from a CO_2 cylinder was fed to the reaction system. The balance of carbon in the catalytic system was estimated to be 98.5 ± 1.5%. HCl and Cl_2 concentrations were analyzed using the chemical titration method [16]. The detailed chemical analysis procedures are described in the Supplementary material.

3. Results and discussion

3.1. Physical property

Fig. 1 shows XRD patterns of the 3DOM CeO_2, 0.91Au/3DOM CeO_2, 0.86Pd/3DOM CeO_2, 0.46AuPd$_{1.92}$/3DOM CeO_2, 0.93AuPd$_{1.89}$/3DOM CeO_2, 1.41AuPd$_{1.82}$/3DOM CeO_2, and 2.85AuPd$_{1.87}$/3DOM CeO_2 samples. By referring to XRD pattern of the standard CeO_2 sample (JCPDS PDF# 34-0394), we can realize that XRD lines of the 0.91Au/3DOM CeO_2, 0.86Pd/3DOM CeO_2, and xAuPd$_y$/3DOM CeO_2 samples could be well indexed, as indicated in Fig. 1g. The diffraction peaks at $2\theta = 28.6°, 33.2°, 47.6°, 56.3°, 59.4°, 69.7°, 76.9°$, and $79.1°$ belonged to the (111), (200), (220), (311), (222), (400), (331), and (420) crystal planes of the cubic CeO_2 phase, respectively. It should be pointed out
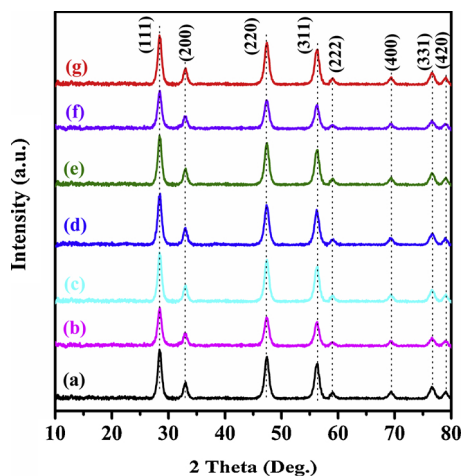

Fig. 1. XRD patterns of (a) 3DOM CeO_2, (b) 0.91Au/3DOM CeO_2, (c) 0.86Pd/3DOM CeO_2, (d) 0.46AuPd$_{1.85}$/3DOM CeO_2, (e) 0.93AuPd$_{1.89}$/3DOM CeO_2, (f) 1.41AuPd$_{1.82}$/3DOM CeO_2, and (g) 2.85AuPd$_{1.87}$/3DOM CeO_2.
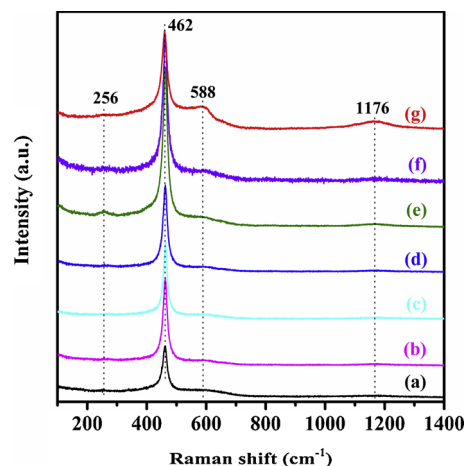

Fig. 2. Raman spectra of (a) 3DOM CeO_2, (b) 0.91Au/3DOM CeO_2, (c) 0.86Pd/3DOM CeO_2, (d) 0.46AuPd$_{1.85}$/3DOM CeO_2, (e) 0.93AuPd$_{1.89}$/3DOM CeO_2, (f) 1.41AuPd$_{1.82}$/3DOM CeO_2, and (g) 2.85AuPd$_{1.87}$/3DOM CeO_2.

that there were no characteristic diffraction peaks of the noble metal phases, indicative of high dispersion of the noble metal NPs on the sample surface. No detection of the noble metal phases might also be owing to their low loadings.

In order to further investigate phase structures of the samples, we measured their Raman spectra, as shown in Fig. 2. It can be seen that there were an intense band at 462 cm^{-1} (due to the Raman mode with a F_{2g} symmetry in the cubic structure of CeO_2) and a weak band at 1176 cm^{-1} (due to the second-order phonon mode) [17]; in addition, two weak bands at 588 and 256 cm^{-1} were recorded, in which the one at 588 cm^{-1} was associated with the oxygen vacancies due to Ce^{3+} presence in the lattice of CeO_2, whereas the one at 256 cm^{-1} was due to displacement of the oxygen atoms from their ideal fluorite lattice positions to the tetragonal positions, which suggests existence of a defect structure. The peak intensity analysis was carried out to estimate the concentration of the oxygen vacancies by comparing the relative intensity (I_{588}/I_{462}) of the Raman bands at 588 and 462 cm^{-1}, and the calculation results show that the 2.85AuPd$_{1.87}$/3DOM CeO_2 sample possessed the highest oxygen vacancy concentration [18,19]. With increasing the Au, Pd or AuPd$_y$ loading, intensity of the band at 588 cm^{-1} increased, indicating a rise in oxygen vacancy concentration [17,20]. According to the literature [11,21], oxygen vacancies could favor the redox reactions and thus promote deep oxidation of CVOCs over the catalysts.

The SEM, TEM, and HAADF–STEM techniques were used to study morphologies and pore structures of the typical samples, and their images are shown in Figs. 3–5, respectively. The 3DOM CeO_2, 0.91Au/3DOM CeO_2, 0.86Pd/3DOM CeO_2, 0.46AuPd$_{1.92}$/3DOM CeO_2, 0.93AuPd$_{1.89}$/3DOM CeO_2, 1.41AuPd$_{1.82}$/3DOM CeO_2, and 2.85AuPd$_{1.87}$/3DOM CeO_2 samples displayed a high-quality 3DOM architecture with a pore size of 160–190 nm (Fig. 3). The macrostructures of the samples were examined by the TEM technique (Fig. 4), and the results show that interconnected macropores within a nanocrystalline skeleton of each sample were generated, in good agreement with the SEM observations. By estimating the sizes of 200 NPs in the TEM images (Fig. 4), we can realize that the sizes (2.9–3.5 nm) of AuPd$_y$ alloy NPs in xAuPd$_y$/3DOM CeO_2 were similar to those (3.1–3.2 nm) of Au or Pd NPs in 0.91Au/3DOM CeO_2 or 0.86Pd/3DOM CeO_2 (Table 1 and Fig. S1). The lattice spacing (d value) was measured to be 0.270 nm, in good consistency with that of the (200) plane of the standard CeO_2 sample. The d value of Au NPs in 0.91Au/3DOM CeO_2 was 0.235 nm, which was assigned to the (111) crystal face (Fig. 4c). The d value of Pd NPs in 0.86Pd/3DOM CeO_2 was 0.226 nm (Fig. 4e), rather close to that of the (111) crystal plane of the standard Pd sample. The hemispherical AuPd$_y$ NPs supported on the surface of 3DOM CeO_2
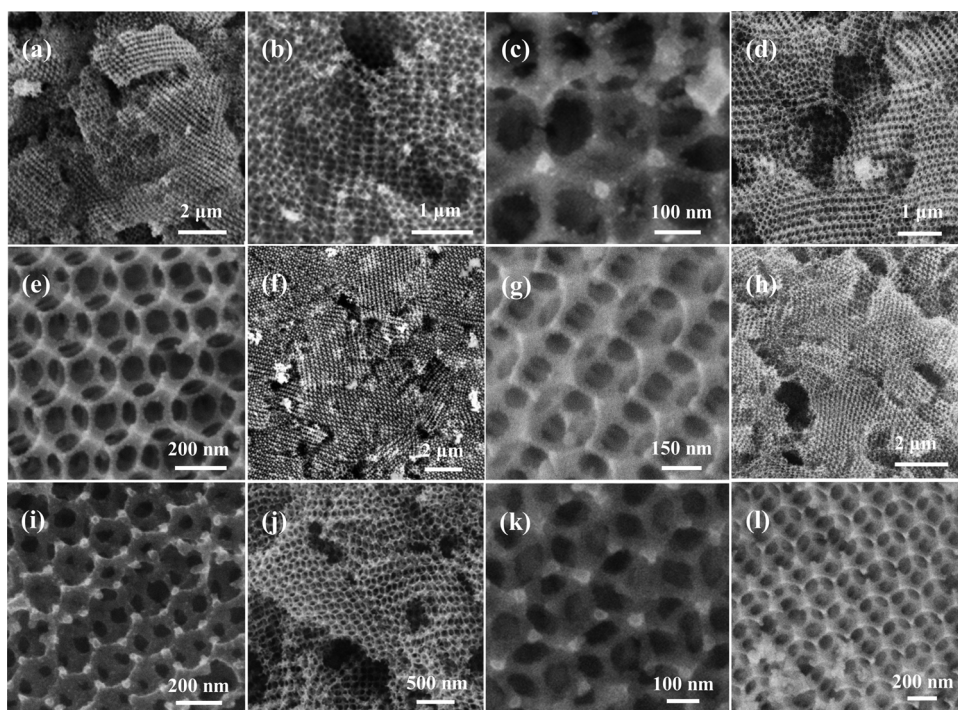
Fig. 3. SEM images of (a) 3DOM CeO$_2$, (b, c) 0.91Au/3DOM CeO$_2$, (d, e) 0.86Pd/3DOM CeO$_2$, (f, g) 0.46AuPd$_{1.85}$/3DOM CeO$_2$, (h, i) 0.93AuPd$_{1.89}$/3DOM CeO$_2$, (j, k) 1.41AuPd$_{1.82}$/3DOM CeO$_2$, and (l) 2.85AuPd$_{1.87}$/3DOM CeO$_2$.

clearly exhibited well-resolved lattice fringes with a *d* value of 0.231 nm, which was attributed to the fcc (111) crystal face of AuPd$_y$ NPs (Fig. 4g, i, and k). To further investigate structures and compositions of the *x*AuPd$_y$/3DOM CeO$_2$ samples, we recorded the HAADF–STEM images and EDS elemental mappings (Fig. 5) of 2.85AuPd$_{1.87}$/3DOM CeO$_2$. It can be clearly seen from Fig. 5 that signal intensity of the Au element (sapphirine in color) was almost the same as that of the

Pd element (green in color), implying that Au and Pd were well mixed in the AuPd$_y$ NPs. Such a well-mixed structure was an indication of Au alloyed with Pd in the AuPd$_y$ NPs, and these Au–Pd alloy NPs were uniformly dispersed on the surface of 3DOM CeO$_2$ [13]. The synergic effect of AuPd$_y$ alloys and 3DOM CeO$_2$ could provide the active sites for adsorption and activation of molecular oxygen.

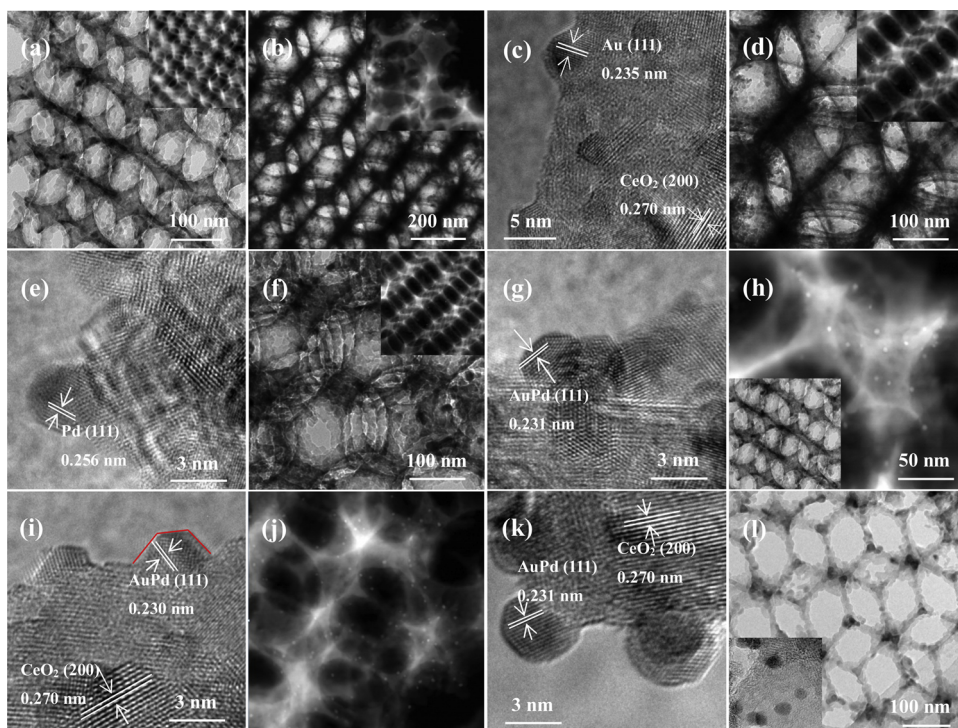Fig. S2 shows the N$_2$ adsorption–desorption isotherms and pore-size

Fig. 4. TEM images of (a) 3DOM CeO$_2$, (b, c) 0.91Au/3DOM CeO$_2$, (d, e) 0.86Pd/3DOM CeO$_2$, (f, g) 0.46AuPd$_{1.85}$/3DOM CeO$_2$, (h, i) 0.93AuPd$_{1.89}$/3DOM CeO$_2$, (j, k) 1.41AuPd$_{1.82}$/3DOM CeO$_2$, and (l) 2.85AuPd$_{1.87}$/3DOM CeO$_2$.
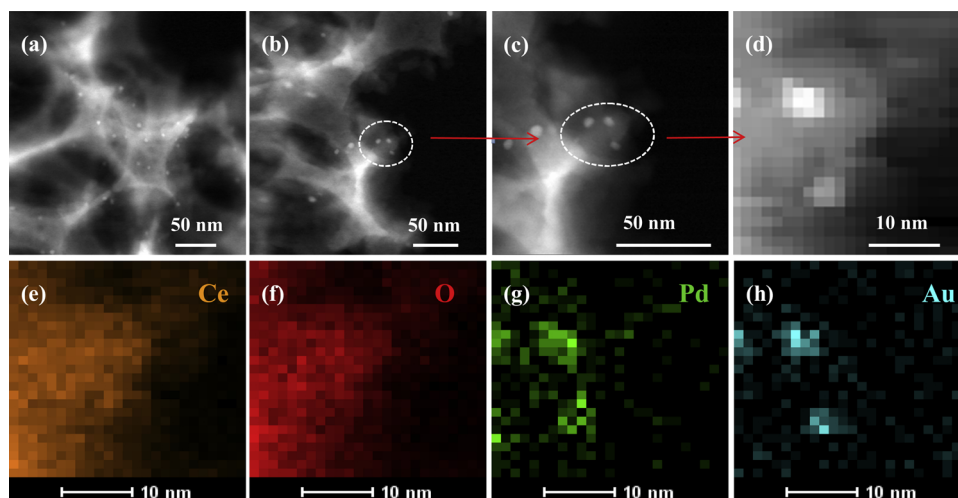
Fig. 5. (a–d) HAADF–STEM images and (e–h) EDS elemental mappings of the 2.85AuPd$_{1.87}$/3DOM CeO$_2$ sample.

distributions of the 3DOM CeO$_2$, 0.91Au/3DOM CeO$_2$, 0.86Pd/3DOM CeO$_2$, 0.46AuPd$_{1.92}$/3DOM CeO$_2$, 0.93AuPd$_{1.89}$/3DOM CeO$_2$, 1.41AuPd$_{1.82}$/3DOM CeO$_2$, and 2.85AuPd$_{1.87}$/3DOM CeO$_2$ samples. Each of the samples presents a type II isotherm with an H3 hysteresis loop in the relative pressure (p/p_0) range of 0.8–1.0 and a small H2 type hysteresis loop in the p/p_0 range of 0.2–0.8. The appearance of a H3 hysteresis loop was an indication of macropore formation in the materials. The H2 hysteresis loop in the p/p_0 range of 0.2–0.8 indicates presence of mesopores in the skeleton of 3DOM CeO$_2$ [22,23]. Therefore, mesopores (2.5–4.3 nm) and macropores (160–190 nm) co-existed in these samples (Table 1), as confirmed by the SEM and TEM observations and pore-size distributions of the 3DOM samples. The mesopores were formed due to aggregation of CeO$_2$ NPs on the skeleton walls. Surface areas (35.6–37.7 m^2/g) of the 0.91Au/3DOM CeO$_2$, 0.86Pd/3DOM CeO$_2$, and xAuPd$_y$/3DOM TiO$_2$ samples were slightly lower than that (42.3 m^2/g) of the 3DOM TiO$_2$ support, and all of the samples possessed a pore volume of 0.201–0.210 cm^3/g (Table 1).

3.2. Surface property

XPS measurements were conducted to elucidate surface properties of the samples. Au 4f, Pd 3d, O 1s, and Ce 3d XPS spectra of the 3DOM CeO$_2$, 0.91Au/3DOM CeO$_2$, 0.86Pd/3DOM CeO$_2$, 0.46AuPd$_{1.92}$/3DOM CeO$_2$, 0.93AuPd$_{1.89}$/3DOM CeO$_2$, 1.41AuPd$_{1.82}$/3DOM CeO$_2$, and 2.85AuPd$_{1.87}$/3DOM CeO$_2$ samples and their quantitative analysis results are shown in Fig. 6 and Table 2, respectively. The Au 4f spectrum of each of the Au-containing samples was decomposed to four components (Fig. 6A): the ones at BE = 83.4 and 87.3 eV were due to the surface Au^0 species, while the ones at BE = 84.3, 85.8, 88.4, and 89.9 eV were due to the surface Au$^{\delta+}$ species [24]. Surface Au$^{\delta+}$/Au^0 molar ratios (0.29–0.44) of the supported AuPd$_y$ alloy samples were higher than that (0.30) of the supported Au sample (Table 2). The Pd 3d XPS spectrum of each of the Pd-containing samples could be deconvoluted into four components (Fig. 6B): the ones at BE = 335.5 and 340.7 eV were ascribable to the surface Pd^0 species, whereas the ones at BE = 337.8 and 342.7 eV were attributable to the surface Pd^{2+} species [25]. Surface Pd^{2+}/Pd^0 molar ratios (0.36–0.48) of the xAuPd$_y$/3DOM CeO$_2$ samples were higher than that (0.32) of the 0.89Pd/3DOM CeO$_2$ sample. The results demonstrate that Au addition enhanced surface Pd^{2+} concentration of the sample. With a rise in noble metal loading, surface Au$^{\delta+}$/Au^0 and Pd^{2+}/Pd^0 molar ratios increased (Table 2) and the highest values (0.44 and 0.48) were achieved on the surface of 2.85AuPd$_{1.87}$/3DOM CeO$_2$. It is well known that a higher Au$^{\delta+}$/Au^0 molar ratio stands for a stronger ability in activating oxygen molecules. The active Au$^{\delta+}$ and Pd^{2+} species located at the interface between AuPd$_y$ NPs and CeO$_2$ were beneficial for improving O$_2$ adsorption and

activation, leading to an increase in amount of the active oxygen species. Therefore, the alloying of Pd with gold could enhance activity for the oxidation of VOCs. The asymmetric O 1s XPS signal was decomposed into three components at BE = 529.6, 531.7, and 533.3 eV (Fig. 6C), assignable to the surface lattice oxygen (O$_{latt}$), adsorbed oxygen (O$_{ads}$, e.g., O$_2^-$, O$_2^{2-}$ or O$^-$), and carbonate or adsorbed water species [26], respectively. It is generally believed that the higher the surface oxygen vacancy density, the easier the activation adsorption of O$_2$ molecules to the electrophilic O$_{ads}$ species (which would play an important role in deep oxidation of VOCs. By quantitatively analyze the O 1s XPS spectra of the samples (Table 2), we can realize that surface O$_{ads}$/O$_{latt}$ molar ratio decreased in the order of 2.85AuPd$_{1.87}$/3DOM CeO$_2$ (0.59) > 1.41AuPd$_{1.82}$/3DOM CeO$_2$ (0.55) > 0.93AuPd$_{1.89}$/3DOM CeO$_2$ (0.54) > 0.86Pd/3DOM CeO$_2$ (0.52) > 0.46AuPd$_{1.92}$/3DOM CeO$_2$ (0.50) > 0.91Au/3DOM CeO$_2$ (0.47) > 3DOM CeO$_2$ (0.42), in good agreement with their O$_2$-TPD results (shown below). In the Ce 3d XPS spectra of the samples (Fig. 6D), there were two sets of Ce 3d$_{3/2}$ components at BE = 901.4, 902.9, 908.0, and 917.0 eV, and Ce 3d$_{5/2}$ components at BE = 882.7, 884.8, 889.4, and 898.7 eV. The components at BE = 884.8 and 902.9 eV were assignable to the surface Ce^{3+} species, whereas the other components were attributable to the surface Ce^{4+} species [22]. This result indicates that cerium on the surface of each sample existed in a mixed oxidation state of Ce^{3+} and Ce^{4+}. For the charge compensation, there was formation of oxygen vacancies in the surface of CeO$_2$, which was beneficial for generation of the active oxygen species. The XPS results reveal that loading Au and Pd gave rise to the enhancement in surface Ce^{3+} concentration, suggesting that there was a strong interaction between AuPd$_y$ NPs and 3DOM CeO$_2$.

To examine the effect of Au and Pd oxidation states on catalytic performance, we recorded XPS Au 4f, Pd 3d, O 1s, and Ce 3d spectra of the 2.85AuPd$_{1.87}$/3DOM CeO$_2$ sample that was treated in H$_2$, N$_2$, and air, respectively, as shown in Fig. S3. Surface element compositions of 2.85AuPd$_{1.87}$/3DOM CeO$_2$ after treatments in different atmospheres are summarized in Table S1. When the 2.85AuPd$_{1.87}$/3DOM CeO$_2$ sample was pretreated in H$_2$, N$_2$, and air at 550 °C for 2 h, respectively, the surface molar ratios of Au$^{\delta+}$/Au^0 (0.31–0.48), Pd^{2+}/Pd^0 (0.34–0.48), Ce^{3+}/Ce^{4+} (0.23–0.27), and O$_{ads}$/O$_{latt}$ (0.55–0.59) did not change significantly. After pretreatment of this sample in air at 550 °C for 2 h, the surface molar ratios of Au$^{\delta+}$/Au^0 (0.44), O$_{ads}$/O$_{latt}$ (0.59), and Pd^{2+}/Pd^0 (0.48) increased considerably, although those of Ce^{3+}/Ce^{4+} (0.24) increased slightly. Catalytic TCE oxidation activity decreased in the order of 2.85AuPd$_{1.87}$/3DOM CeO$_2$ pretreated in air > 2.85 AuPd$_{1.87}$/3DOM CeO$_2$ pretreated in N$_2$ ≈ 2.85AuPd$_{1.87}$/3DOM CeO$_2$ pretreated in H$_2$ (Fig. 12). As shown in Fig. S3(B), Pd 3d XPS peaks of the 2.85AuPd$_{1.87}$/3DOM CeO$_2$ pretreated in H$_2$ were obviously shifted to the lower BEs, as compared with those of the samples pretreated in
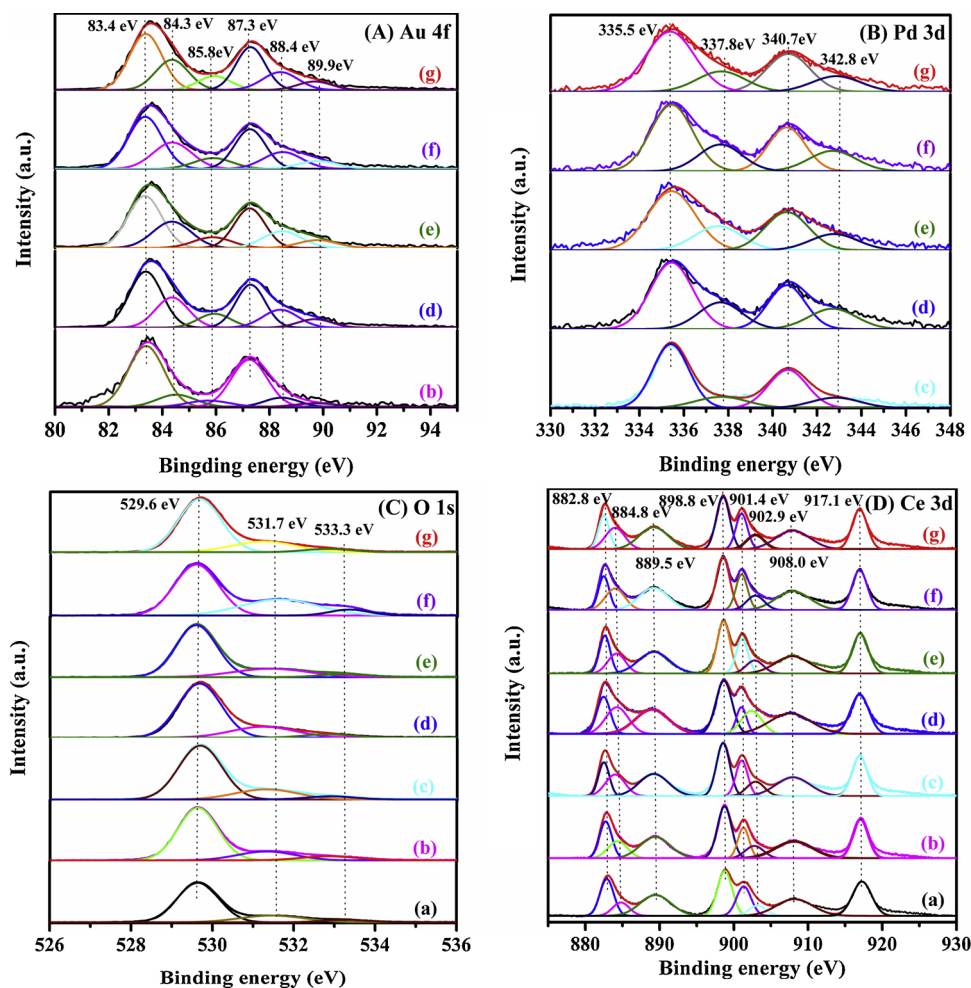
Fig. 6. (A) Au 4f, (B) Pd 3d, (C) O 1s, and (D) Ce 3d XPS spectra of (a) 3DOM CeO$_2$, (b) 0.91Au/3DOM CeO$_2$, (c) 0.86Pd/3DOM CeO$_2$, (d) 0.46AuPd$_{1.85}$/3DOM CeO$_2$, (e) 0.93AuPd$_{1.89}$/3DOMCeO$_2$, (f) 1.41AuPd$_{1.82}$/3DOM CeO$_2$, and (g) 2.85AuPd$_{1.87}$/3DOM CeO$_2$.

air and N$_2$, which was a result due to reduction of palladium by hydrogen. It was reported that pretreatment in air or O$_2$ can increase the O$_{ads}$ species concentration on the surface of an oxygen-deficient catalyst [27]. Therefore, oxygen vacancy might be one of factors influencing the TCE oxidation activity of the 2.85AuPd$_{1.87}$/3DOM CeO$_2$ sample.

It should be pointed out that the surface Au, Pd or Au–Pd NPs might facilitate the reduction of Ce^{4+} to Ce^{3+} and oxidation of Au^0 to Au$^{\delta+}$

(Au^0 + Ce^{4+} → Au$^{\delta+}$ + Ce^{3+}) and Pd^0 to Pd^{2+} (Pd^0 + Ce^{4+} → Pd^{2+} + Ce^{3+}) at the Au–CeO$_2$, Pd–CeO$_2$ or AuPd$_y$–CeO$_2$ interfaces, resulting in increases in surface Ce^{3+}, Au$^{\delta+}$, Pd^{2+}, and O$_{ads}$ species concentrations. Formation of the surface Ce^{3+} species could favor generation of oxygen vacancies, O$_{ads}$ species on the surface of CeO$_2$, and hence improvement in catalytic activity (shown below), whereas formation of Au$^{\delta+}$ and Pd^{2+} could promote oxidation of TCE and thus enhancement

Table 2
Surface element compositions, O$_2$ desorption, and H$_2$ consumption of the samples.

Sample	Surface element composition[a]			O$_2$ desorption[b] (mmol/g)				H$_2$ consumption[c] (mmol/g)		
	Au$^{\delta+}$/Au^{0}molar ratio	Pd^{2+}/Pd^0 molar ratio	O$_{ads}$/O$_{latt}$ molar ratio	50–300 °C	300–500 °C	500–900 °C	Total	< 550 °C	≥ 550 °C	Total
3DOM CeO$_2$	–	–	0.42	0.46	0.24	0.95	1.65	0.21	0.65	0.86
0.91Au/3DOM CeO$_2$	0.30	–	0.47	–	–	–	–	0.25	0.80	1.05
0.86Pd/3DOM CeO$_2$	–	0.32	0.52	–	–	–	–	0.37	0.83	1.20
0.46AuPd$_{1.85}$/3DOM CeO$_2$	0.29	0.36	0.50	1.19	0.47	0.98	2.64	0.28	0.79	1.07
0.93AuPd$_{1.89}$/3DOM CeO$_2$	0.33	0.39	0.54	1.22	0.71	0.83	2.76	0.31	0.98	1.29
1.41AuPd$_{1.82}$/3DOM CeO$_2$	0.39	0.41	0.55	1.23	0.73	1.14	3.10	0.45	0.87	1.32
2.85AuPd$_{1.87}$/3DOM CeO$_2$	0.44	0.48	0.59	1.31	0.78	1.96	4.05	0.73	0.74	1.47

[a] Data were estimated by quantitatively analyzing the XPS spectra of the samples.
[b] Data were calculated by quantitatively analyzing the O$_2$-TPD profiles of the samples.
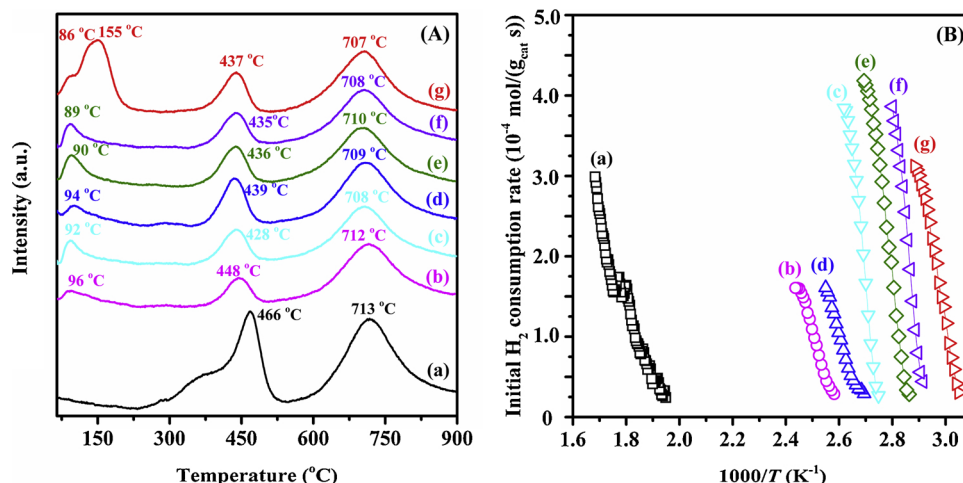[c] Data were obtained by quantitatively analyzing the H$_2$-TPR profiles.

Fig. 7. (A) H_2-TPR profiles and (B) initial H_2 consumption rate versus inverse temperature of (a) 3DOM CeO_2, (b) 0.91Au/3DOM CeO_2, (c) 0.86Pd/3DOM CeO_2, (d) 0.46AuPd$_{1.85}$/3DOM CeO_2, (e) 0.93AuPd$_{1.89}$/3DOM CeO_2, (f) 1.41AuPd$_{1.82}$/3DOM CeO_2, and (g) 2.85AuPd$_{1.87}$/3DOM CeO_2.

in catalytic performance (shown below) of the samples.

3.3. Low-temperature reducibility, oxygen species, and surface acidity

H_2-TPR experiments were carried out to study the reducibility of the 3DOM CeO_2, 0.91Au/3DOM CeO_2, 0.86Pd/3DOM CeO_2, 0.46AuPd$_{1.92}$/3DOM CeO_2, 0.93AuPd$_{1.89}$/3DOM CeO_2, 1.41AuPd$_{1.82}$/3DOM CeO_2, and 2.85AuPd$_{1.87}$/3DOM CeO_2 samples, and their profiles are shown in Fig. 7A. The 3DOM CeO_2 sample exhibited two reduction peaks at 466 and 713 °C: The former was associated with reduction of Ce^{4+} in the outmost layer to Ce^{3+} and removal of the adsorbed oxygen species, whereas the latter was due to reduction of the inner Ce^{4+} to Ce^{3+} and lattice oxygen species [28]. With the loading of Au, Pd or AuPd$_y$ NPs on 3DOM CeO_2, three or four reduction peaks appeared at different temperatures, depending upon the noble metal contents. The reduction peaks shifted to lower temperatures (428–448 and 707–712 °C), suggesting that the reduction of 3DOM CeO_2 was promoted by the noble metal NPs via the strong interaction of noble metal NPs with 3DOM CeO_2. Similar phenomena were also observed in the Au–Pd/3DOM Mn_2O_3 [29] and Au–Pd/3DOM Co_3O_4 [13] catalysts. The peak at low temperature was owing to reduction of the oxidized noble metals and removal of the adsorbed oxygen species on the xAuPd$_y$/3DOM CeO_2 surface. The strong interaction between 3DOM CeO_2 and noble metal NPs could enhance mobility of the surface active oxygen species, which was beneficial for destruction of the reactants and by-products produced during the CVOC oxidation process. By quantitatively analyzing the H_2-TPR profiles, we can obtain the H_2 consumption of the samples. The H_2 consumption (0.86 mmol/g) of 3DOM CeO_2 was lower than that (1.05–1.47 mmol/g) of xAuPd$_y$/3DOM CeO_2 (Table 2). The H_2 consumption below 550 °C decreased in the sequence of 2.85AuPd$_{1.87}$/3DOM CeO_2 (0.73 mmol/g) > 1.41AuPd$_{1.82}$/3DOM CeO_2 (0.45 mmol/g) > 0.86Pd/3DOM CeO_2 (0.37 mmol/g) > 0.93AuPd$_{1.89}$/3DOM CeO_2 (0.31 mmol/g) > 0.46AuPd$_{1.92}$/3DOM CeO_2 (0.28 mmol/g) > 0.91Au/3DOM CeO_2 (0.25 mmol/g) > 3DOM CeO_2 (0.21 mmol/g), in basic consistency with the order in catalytic activity. The improvement in low-temperature reducibility of the sample could enhance catalytic activity for VOCs oxidation [30]. Apparently, the 2.85AuPd$_{1.87}$/3DOM CeO_2 showed the lowest reduction temperature (88 °C), i.e., this sample possessed the best low-temperature reducibility. The H_2 consumption rate was used to better evaluate the low-temperature reducibility (less than 25% oxygen corresponding to the first reduction peak of the sample was consumed [31]), and the results are shown in Fig. 7B. It is seen that the initial H_2 consumption rate (i.e., low-temperature reducibility) decreased in the order of 2.85AuPd$_{1.87}$/3DOM CeO_2 > 1.41AuPd$_{1.82}$/3DOM CeO_2 > 0.93AuPd$_{1.89}$/3DOM CeO_2 > 0.86Pd/3DOM CeO_2 > 0.46AuPd$_{1.92}$/3DOM CeO_2 > 0.91Au/3DOM CeO_2 > 3DOM

CeO_2, in good agreement with the sequence in catalytic activity.

Fig. 8 shows O_2-TPD profiles of the 3DOM CeO_2, 0.46AuPd$_{1.92}$/3DOM CeO_2, 0.93AuPd$_{1.89}$/3DOM CeO_2, 1.41AuPd$_{1.82}$/3DOM CeO_2, and 2.85AuPd$_{1.87}$/3DOM CeO_2 samples. There were three oxygen desorption peaks at 120, 410, and 670 °C. It is known that transformation of oxygen follows a sequence of the physically adsorbed O_2 → chemically adsorbed O_2^- → chemically adsorbed O_2^{2-} → chemically adsorbed O^- → surface lattice O^{2-} [32]. The O_2^-, O_2^{2-} or O^- species could not be differentiated on the basis of desorption temperature since they were desorbed at almost similar temperatures, hence the low-temperature peak was roughly assigned to desorption of the chemisorbed O_{ads} species, whereas the high-temperature peak was attributed to desorption of the O_{latt} species. The Raman active O_2^- species [29] were confirmed by recording of the band at 1176 cm^{-1} (Fig. 2). Loading of Au, Pd or AuPd$_y$ NPs resulted in the enhancement in adsorption and desorption of oxygen (Table 2). The AuPd$_y$ alloy NPs possessed a strong electron donating ability, which would favor the adsorption and activation of oxygen molecules. It can be seen from Table 2 that amount of the desorbed oxygen species below 500 °C decreased in the order of 2.85AuPd$_{1.87}$/3DOM CeO_2 (2.09 mmol/g) > 1.41AuPd$_{1.82}$/3DOM CeO_2 (1.96 mmol/g) > 0.93AuPd$_{1.89}$/3DOM CeO_2 (1.93 mmol/g) > 0.46AuPd$_{1.92}$/3DOM CeO_2 (1.66 mmol/g) > 3DOM CeO_2 (0.70 mmol/g), with the 2.85AuPd$_{1.87}$/3DOM CeO_2 sample possessing the highest amount of oxygen desorption.

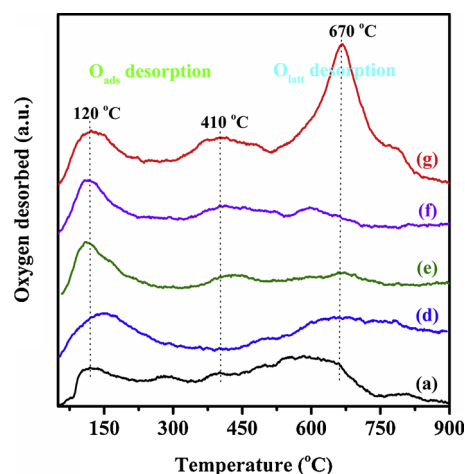We used the NH$_3$-TPD technique to measure surface acid properties

Fig. 8. O_2-TPD profiles of (a) 3DOM CeO_2, (d) 0.46AuPd$_{1.85}$/3DOM CeO_2, (e) 0.93AuPd$_{1.89}$/3DOM CeO_2, (f) 1.41AuPd$_{1.82}$/3DOM CeO_2, and (g) 2.85AuPd$_{1.87}$/3DOM CeO_2.

of the 3DOM CeO_2 and 2.85$AuPd_{1.87}$/3DOM CeO_2 samples, and their profiles are illustrated in Fig. S4. The desorption peak at 50–450 °C was assigned to the successive desorption of ammonia physically adsorbed at the weak Brønsted acid sites in each of the samples. The peaks at 450–900 °C were due to desorption of ammonia chemically adsorbed at the strong acid sites. Additionally, there were desorption peaks centered at 120 and 324 °C for the two samples, which could be attributed to decomposition of NH_4^+ ions at the Brønsted acid sites. In addition, there were peaks at 450–900 °C, which were due to desorption of the coordinated NH_3 molecules at the Lewis acid sites. For the 2.85$AuPd_{1.87}$/3DOM CeO_2 sample, however, intensity of the desorption peaks increased (as compared with that of the 3DOM CeO_2 sample), which was possibly due to the synergetic effect between $AuPd_y$ NPs and 3DOM CeO_2. NH_3 desorption from the 3DOM CeO_2 sample was weaker in peak intensity than that from the 2.85$AuPd_{1.87}$/3DOM CeO_2 sample, indicating a lower amount of NH_3 adsorption on the former sample. Acid amounts of the samples were estimated according to the relative area (A_{strong}/A_{weak}) of the desorption peaks [33,34]. It can be clearly seen from Table S2 that amount (A_{strong}/A_{weak} = 2.40) of the strong acid sites in 2.85$AuPd_{1.87}$/3DOM CeO_2 was much more than that (A_{strong}/A_{weak} = 0.34) in 3DOM CeO_2, suggesting that $AuPd_y$ loading could enhance acidity of the sample. With the loading of $AuPd_y$ alloy NPs, amounts of the weak and strong acid sites increased. Furthermore, the 2.85$AuPd_{1.87}$/3DOM CeO_2 sample displayed larger peak areas than the 3DOM CeO_2 sample at high temperatures, indicating that there was a more amount of the Lewis acid sites on the surface of the former. As reported in the literature [35], amount of the Lewis acid sites played a significant role in enhancing the activity, and the strong acid sites were more important than the weak acid sites in deep oxidation of CVOCs, but the weak acid sites were associated with the adsorption of CVOCs.

3.4. Desorption and surface reaction of TCE

TCE adsorption ability is one of the key factors influencing catalytic performance of the samples. In general, the higher desorption temperature and higher peak intensity indicate a stronger adsorption of VOC molecules on the surface active sites of a catalyst. Fig. 9 shows the TCE-TPD profiles of the 3DOM CeO_2 and 2.85$AuPd_{1.87}$/3DOM CeO_2 samples. There were four desorption peaks in the temperature range of 50–900 °C. The weak peak below 500 °C was attributed to desorption of the physically or weakly chemically adsorbed TCE, whereas the one above 500 °C was assigned to desorption of the strongly chemically adsorbed TCE [36]. The 2.85$AuPd_{1.87}$/3DOM CeO_2 sample showed TCE desorption peaks below and above 500 °C with higher intensity, as compared with the 3DOM $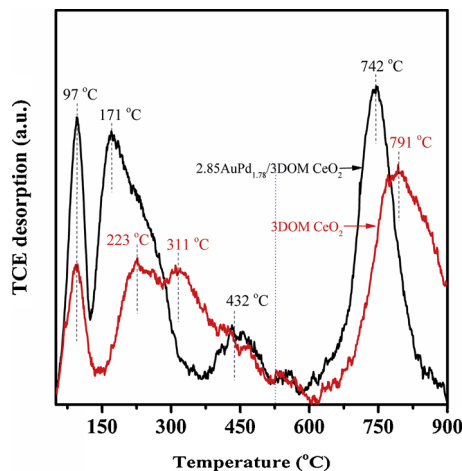CeO_2$ sample. This result indicates that there was a more amount of TCE adsorption on the former than that on the latter, which was in agrreement with the changing trend in ammonia desorption from the Brønsted acid sites (Fig. 8). Taking into account the importance of reactant adsorption ability, we believe that the good catalytic performance of 2.85$AuPd_{1.87}$/3DOM CeO_2 for TCE oxidation was associated with its activated adsorption of oxygen and TCE.

The TPSR technique was used to investigate desorption–oxidation behaviors of TCE over the 3DOM CeO_2 and 2.85$AuPd_{1.87}$/3DOM CeO_2 samples at 100–900 °C, and their results are shown in Fig. S5. The change in intensity of the peaks reflected the alteration in concentration of the reactant (or product). The formed reaction products were mainly CO_2, CO, HCl, PCE (perchloroethylene), and Cl_2. The destruction of desorbed TCE occurred at lower temperatures. Formation of CO_2 and CO over the 3DOM CeO_2 and 2.85$AuPd_{1.87}$/3DOM CeO_2 samples was distinctly different, which were analyzed online during the reaction process. As compared with the amount of produced CO_2 over 3DOM CeO_2, that over 2.85$AuPd_{1.87}$/3DOM CeO_2 increased obviously, which suggests that the interaction between $AuPd_{1.87}$ NPs and 3DOM CeO_2 promoted the deep oxidation of TCE to CO_2. A small amount of CO was detected over 2.85$AuPd_{1.87}$/3DOM CeO_2, however, an appreciable CO amount was observed over 3DOM CeO_2. In the low-temperature range, desorption of the physically adsorbed HCl was observed over the 3DOM CeO_2 and 2.85$AuPd_{1.87}$/3DOM CeO_2 samples, but only trace amount of Cl_2 was detected over both samples. Due to its strong oxidizing ability of the 2.85$AuPd_{1.87}$/3DOM CeO_2 sample, the desorption of HCl increased with a rise in temperature. The main Cl-containing hydrocarbon product was PCE. At 200 − 400 °C, the amount of PCE generated over the $AuPd_y$-loaded sample was higher, indicating that the main reaction occurring at the acid sites was dehydrochlorination [37]. The Cl atoms in TCE could interact with the Lewis acid sites, the surface O_{ads} species or hydroxyl group could attack the carbon atoms in TCE, and the dehydrochlorination of TCE took place.

3.5. Catalytic performance

Fig. 10A shows catalytic activities of the 3DOM CeO_2, 0.91Au/3DOM CeO_2, 0.86Pd/3DOM CeO_2, 0.46$AuPd_{1.92}$/3DOM CeO_2, 0.93$AuPd_{1.89}$/3DOM CeO_2, 1.41$AuPd_{1.82}$/3DOM CeO_2, and 2.85$AuPd_{1.87}$/3DOM CeO_2 samples for TCE combustion. In order to make it easier to compare catalytic activities of the samples, we used the reaction temperatures $T_{10\%}$, $T_{50\%}$, and $T_{90\%}$ (corresponding to TCE conversion = 10, 50, and 90%), as summarized in Table 3. 3DOM CeO_2 exhibited a relatively poor activity with the $T_{10\%}$ of 280 °C, and no data of the $T_{50\%}$, and $T_{90\%}$ could be obtained. After loading of Au, Pd or $AuPd_y$, catalytic activity was remarkably improved. It should be pointed out that the 3DOM structure was beneficial for dispersion of the active components as well as adsorption and diffusion of the reactants and products, and the higher surface area could also provide the reactants to approach the surface active sites more readily. It can be realized from Table 3 that the catalytic activity at SV = 20,000 mL/(g h) decreased in the sequence of 2.85$AuPd_{1.87}$/3DOM CeO_2 ($T_{50\%}$ = 330 °C) > 1.41$AuPd_{1.82}$/3DOM CeO_2 ($T_{50\%}$ = 347 °C) > 0.93$AuPd_{1.89}$/3DOM CeO_2 ($T_{50\%}$ = 350 °C) > 0.86Pd/3DOM CeO_2 ($T_{50\%}$ = 370 °C) > 0.46$AuPd_{1.92}$/3DOM CeO_2 ($T_{50\%}$ = 375 °C) > 0.91Au/3DOM CeO_2 ($T_{50\%}$ = 390 °C) > 3DOM CeO_2 ($T_{50\%}$ > 390 °C), with the 2.85$AuPd_{1.87}$/3DOM CeO_2 sample showing the highest activity. The sequence in catalytic activity of these samples was in good agreement with those in O_{ads}/O_{latt} molar ratio and low-temperature reducibility.

It was reported that the oxidation of CVOCs over Ru/Al_2O_3 [38] obeyed a first-order toward CVOC concentration and zero-order toward O_2 concentration reaction mechanism. Therefore, it is reasonably supposed that TCE oxidation in the presence of excess oxygen would follow a first-order reaction mechanism with respect to TCE concentration (c): $r = -kc = (-A \exp(-E_a/RT))c$, where r is the reaction rate (mol/s), k is the rate constant (s^{-1}), A is the pre-exponential factor, and E_a is the apparent activation energy (kJ/mol). Based on the kinetic

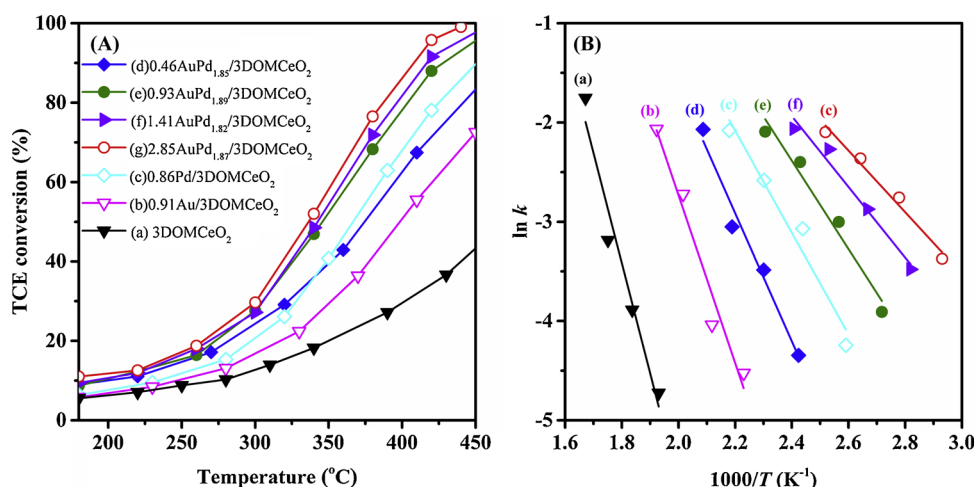**Fig. 9.** TCE-TPD profiles of the 3DOM CeO_2 and 2.85$AuPd_{1.87}$/3DOM CeO_2 samples.

Fig. 10. (A) TCE conversion as a function of temperature and (B) ln k versus inverse temperature over (a) 3DOM CeO$_2$, (b) 0.91Au/3DOM CeO$_2$, (c) 0.86Pd/3DOM CeO$_2$, (d) 0.46AuPd$_{1.85}$/3DOM CeO$_2$, (e) 0.93AuPd$_{1.89}$/3DOM CeO$_2$, (f) 1.41AuPd$_{1.82}$/3DOM CeO$_2$, and (g) 2.85AuPd$_{1.87}$/3DOM CeO$_2$.

measurements (Fig. 10B), the lowest apparent activation energy (E_a) of TCE oxidation over the 2.85AuPd$_{1.87}$/3DOM CeO$_2$ calculated from the corresponding Arrhenius plots at TCE conversion < 20% and SV = 20,000 mL/(g h) was 33 kJ/mol, much lower than that (108 kJ/mol) over 3DOM CeO$_2$ (Tables 3). This result demonstrates that loading of AuPd$_{1.87}$ ally NPs could significantly decrease the E_a of TCE oxidation, and hence enhance the catalytic performance. We calculated the TCE reaction rates (normalized by per gram of noble metal of the catalyst) and turnover frequencies (TOF$_{Noble\ metal}$, defined as TOF$_{Noble\ metal}$ = xC_0/n, where x is the conversion at a certain temperature, C_0 (mol/s) is the initial TCE concentration per second, and n (mol) is the molar amount of noble metal (M = Au, Pd or AuPd$_y$)), as summarized in Table 3. Apparently, the highest TCE reaction rate (11.8 μmol/(g$_{Noble\ metal}$ s)) and the highest TOF$_{Noble\ metal}$ (2.25 × 10^{-3} s^{-1}) at 300 °C were achieved over the 2.85AuPd$_{1.87}$/3DOM CeO$_2$ sample. In recent years, a number of works on TCE oxidation over the different catalysts have been reported in the literature, in which the typical activities are summarized in Table S3. It is seen that the TCE reaction rate (8.5 × 10^{-8} mol/(g$_{cat}$ s)) over 2.85AuPd$_{1.87}$/3DOM CeO$_2$ was much higher than that (3.49 × 10^{-9} mol/(g$_{cat}$ s)) over 0.42 wt% Pd/Al$_2$O$_3$ [39] and that (2.67 × 10^{-9} mol/(g$_{cat}$ s)) over 4.3 wt% Mn/HZSM-5 [40], but inferior to that (1.13 × 10^{-7} mol/(g$_{cat}$ s)) over 1.02 wt% Ru/TiO$_2$ (P25) [41]. CeO$_2$ possesses unique Ce^{4+}/Ce^{3+} redox property that could promote dissociation of the C–Cl bonds. It is well known that Cl tends to be adsorbed on oxygen vacancies of CeO$_2$. Simultaneously, the 3DOM structure with a higher surface area is beneficial for enhancement in adsorption and mass transfer of the reactant molecules, and the nanosized skeleton surface is favorable for improvement in reducibility. The Au, Pd or Au–Pd NPs with a size of 3–4 nm were uniformly dispersed on the skeleton surface of 3DOM CeO$_2$. The strong interaction between noble metals (Au, Pd or Au–Pd) and 3DOM CeO$_2$ resulted in

rises in oxygen vacancy density and O$_{ads}$ concentration, which could modify the chemical environment around oxygen vacancies and hence prohibit adsorption of Cl species. Furthermore, loading of noble metal NPs could increase amount of strong acid sites. Therefore, the O$_{ads}$ species concentration, low-temperature reducibility, strong interaction between noble metal NPs and 3DOM CeO$_2$, and strong acidity were the factors influencing catalytic performance of the samples for TCE combustion.

After analyzing the effluent gases of TCE oxidation, we can know that the reaction products were mainly CO$_2$, CO, H$_2$O, HCl, Cl$_2$, and C$_2$Cl$_4$ (tetrachloroethylene). The C$_2$Cl$_4$ concentration versus temperature over the as-obtained samples at SV = 20,000 mL/(g h) is shown in Fig. S6. Over the 0.91Au/3DOM CeO$_2$, 0.86Pd/3DOM CeO$_2$, 0.46AuPd$_{1.92}$/3DOM CeO$_2$, 0.93AuPd$_{1.89}$/3DOM CeO$_2$, 1.41AuPd$_{1.82}$/3DOM CeO$_2$, and 2.85AuPd$_{1.87}$/3DOM CeO$_2$ samples, we detected the production of C$_2$Cl$_4$ and the maximal C$_2$Cl$_4$ concentrations were < 168 ppm; in addition, a similar distribution of C$_2$Cl$_4$ at 240–500 °C was observed over each of the samples. The HCl selectivities (S_{HCl}) over the samples are summarized in Table 3. Each sample showed a high HCl selectivity. A high HCl selectivity would be favorable for the oxidation of TCE because HCl can be easily treated and less toxic than Cl$_2$. Furthermore, the CO$_x$ (CO$_2$ + CO) selectivity over each sample was above 99% (higher than 98% CO$_2$ and a trace amount of CO). It should be pointed out that the estimated carbon and chlorine balances were 95–98 and 90–94%, respectively. That is to say, small amounts of carbon and chlorine were retained on the surface of the samples.

3.6. Catalytic stability and effects of H$_2$O, HCl, and CO$_2$ on catalytic activity

Stability of the 2.85AuPd$_{1.87}$/3DOM CeO$_2$ sample was examined in

Table 3
Catalytic activities, HCl selectivities (S_{HCl}), reaction rates, turnover frequencies (TOFs), and apparent activation energies (E_a) at SV = 20,000 mL/(g h) of the samples.

Sample	Catalytic activity				Reaction rate at 300 °C	TCE oxidation at 300 °C	E_a
	$T_{10\%}$ (°C)	$T_{50\%}$ (°C)	$T_{90\%}$ (°C)	S_{HCl}[a]	(μmol/(g$_{Noble\ metal}$ s))	TOF$_{Noble\ metal}$ (× 10^{-3} s^{-1})	(kJ/mol)
3DOM CeO$_2$	280	–	–	37.2	–	–	108
0.91Au/3DOM CeO$_2$	240	390	–	88.5	5.2	0.98	91
0.86Pd/3DOM CeO$_2$	178	370	449	89.6	5.9	1.12	53
0.46AuPd$_{1.85}$/3DOM CeO$_2$	235	375	–	92.8	6.8	1.29	42
0.93AuPd$_{1.89}$/3DOM CeO$_2$	185	350	430	91.5	10.6	2.01	37
1.41AuPd$_{1.82}$/3DOM CeO$_2$	186	347	426	92.6	10.9	2.12	36
2.85AuPd$_{1.87}$/3DOM CeO$_2$	165	330	415	93.4	11.8	2.25	33

[a] S_{HCl} = [HCl]/([HCl] + 2[Cl$_2$]), which was measured at 430 °C.

(750 ppm TCE + 20 vol% O_2 + 80 vol% N_2) at 410 °C and SV = 20,000 mL/(g h), as shown in Fig. S7(A). There was nearly no significant loss in activity after 24 h of on-stream reaction. The excellent catalytic stability of the supported $AuPd_{1.87}$ alloy sample might be associated with the strong interaction between $AuPd_{1.87}$ alloy NPs and 3DOM CeO_2. We also examined the morphology change of the used 2.85$AuPd_{1.87}$/3DOM CeO_2 sample, and its TEM images and particle size distribution are shown in Fig. S7(B). It is clearly seen that there was no apparent increase in particle size of $AuPd_{1.87}$ in 2.85$AuPd_{1.87}$/3DOM CeO_2 before and after the recycled test (from 3.3 to 3.8 nm). Simultaneously, the 3DOM structure of CeO_2 was not significantly damaged. Therefore, the 2.85$AuPd_{1.87}$/3DOM CeO_2 sample showed a stable catalytic performance.

Since water is one of the products of TCE oxidation, it hence is of significance to explore the influence of water vapor on catalytic activity of the typical sample. When 3.0 and 5.0 vol% water vapor were introduced to the reaction system, TCE conversions at 420 °C and SV = 20,000 mL/(g h) over the 2.85$AuPd_{1.87}$/3DOM CeO_2 sample decreased by ca. 7 and 12% (Fig. 11A), respectively; after water vapor was cut off, TCE conversions were recovered. Under the conditions of 5.0 vol% H_2O, 360 °C, and SV = 20,000 mL/(g h), TCE conversion over 2.85$AuPd_{1.87}$/3DOM CeO_2 dropped by ca. 10%, and it was restored when water vapor was cut off. The decrease in TCE conversion was due to competitive adsorption of water vapor and TCE as well as O_2 molecules. Gas-phase oxygen molecules could be adsorbed and activated on the Au–Pd active sites to form the O_{ads} species, whereas the TCE molecules adsorbed on the hydroxyl group-covered surface could be hydrated on the acid sites since the strong acid sites favored the hydration. A similar phenomenon was also observed by the other researchers [42]. The above results demonstrate that the partial deactivation due to water vapor introduction was reversible. Fig. 11B shows catalytic activities of the 2.85$AuPd_{1.87}$/3DOM CeO_2 sample in the presence of 100 ppm HCl at 420 °C and SV = 20,000 mL/(g h), from which we can see that only a small loss (ca. 3%) in TCE conversion was observed. Formation of the highly dispersed Au–Pd alloy NPs on the surface of 3DOM CeO_2 could effectively inhibit the adsorption of HCl on the catalyst surface at high temperatures, which might be the main reason why the 2.85$AuPd_{1.87}$/3DOM CeO_2 sample possessed the excellent HCl-resistant performance. Besides, Dai et al. [43] reported that deactivation of the Ce^{3+}/Ce^{4+} active sites due to adsorption of the chlorine species could be prevented by addition of Ru that catalyzed removal of the adsorbed chlorine species via the Deacon reaction. In our present work, the highly dispersed Au–Pd alloy NPs on the 3DOM CeO_2 surface would play a similar role in promoting removal of the adsorbed chlorine species. The effect of 3.0 or 7.0% CO_2 introduction on activity of the 2.85$AuPd_{1.87}$/3DOM CeO_2 sample was examined at 420 °C and SV = 20,000 mL/(g h) (Fig. 11C). The negative effect of CO_2 addition was due to the reason that partial active sites in this sample
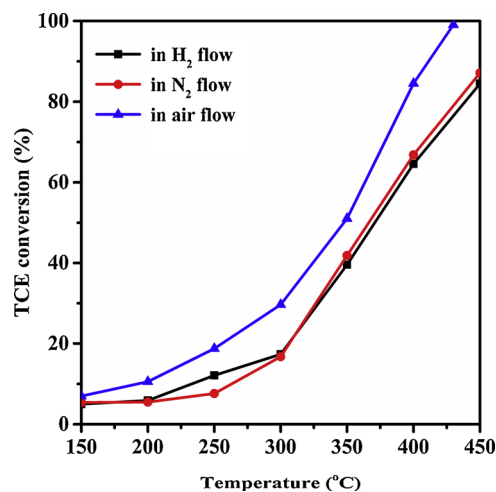

Fig. 12. TCE conversion at SV = 20,000 mL/(g h) over the 2.85$AuPd_{1.87}$/3DOM CeO_2 samples obtained after calcination in a H_2, N_2 or air flow of 50 mL/min at 550 °C for 2 h.

were covered by adsorption of the formed carbonate species [13]. TCE conversion slightly rose when the used sample was treated in O_2 (20 mL/min) at 450 °C for 1 h, which was due to the fact that part of the active sites were still occupied by the carbonate species. Hence, partial deactivation due to CO_2 introduction was irreversible.

3.7. Possible reaction mechanism

We recorded the in situ DRIFT spectra to further investigate the TCE oxidation mechanism over the samples. Fig. S8 shows in situ DRIFTS spectra of the 2.85$AuPd_{1.87}$/3DOM CeO_2 sample after adsorption of (1000 ppm TCE + N_2) at 30 °C for different time. The negative bands in the spectra at 3735, 3690, and 3660 cm^{-1} could be assigned to the OH vibration mode of hydroxyl groups. The bands at 781 and 950 cm^{-1} were related to the C–Cl bonds, the one at 841 cm^{-1} was assigned to the C–H bending vibration of TCE, the ones at 2974, 2940, and 2880 cm^{-1} were attributed to the C–H stretching mode [44], and the ones at 1581 and 1556 cm^{-1} were associated with the C=C bond in TCE [45]. With extension in adsorption time, the featured adsorption bands of TCE increased in intensity at 30 °C. In situ TCE oxidation was carried out in a flow of (1000 ppm TCE + 20 vol% O_2 + 80 vol% N_2) at different temperatures (100–500 °C) over the 3DOM CeO_2 and 2.85$AuPd_{1.87}$/3DOM CeO_2 samples, and their results are shown in Fig. 13A and B, respectively. With the rise in reaction temperature, the intensity of TCE bands became weaker and disappeared gradually, and at the same time some new IR bands appeared. The absorption bands at 3735, 3690, and 3660 cm^{-1} were assigned to the OH vibration mode of hydroxyl group
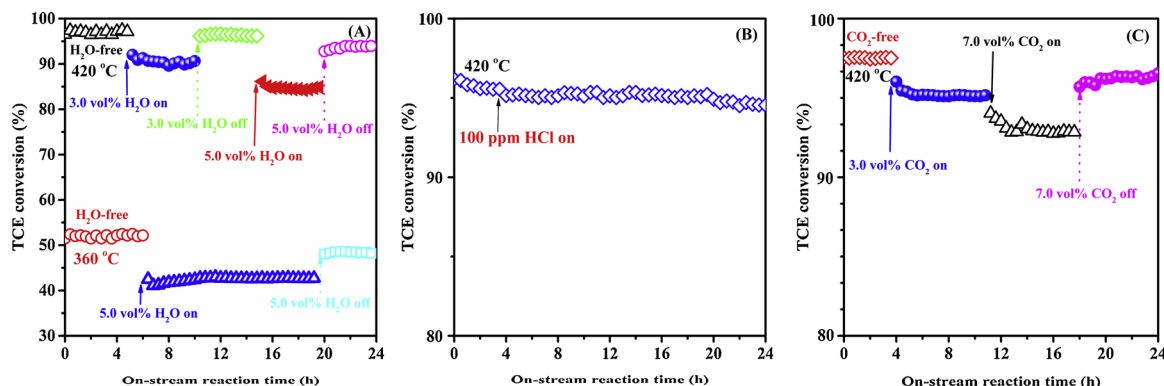

Fig. 11. Effects of (A) water vapor, (B) hydrochloric acid, and (C) carbon dioxide on TCE oxidation over 2.85$AuPd_{1.87}$/3DOM CeO_2 at 420 °C and SV = 20,000 mL/(g h).
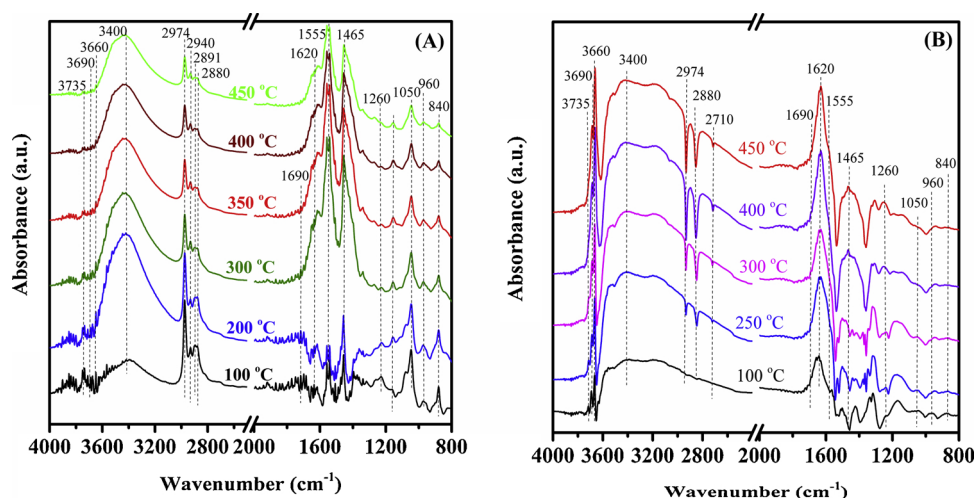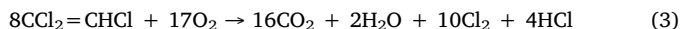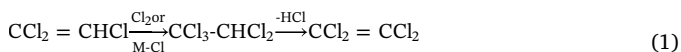
Fig. 13. In situ DRIFT spectra of (A) 2.85AuPd$_{1.87}$/3DOM CeO$_2$ and (B) 3DOM CeO$_2$ during 1000-ppm TCE oxidation at different temperatures.

[46]. There was a broad band at 3400 cm^{-1} due to the surface hydroxyl group [47]. The bands at 2974, 2940, and 2891 cm^{-1} were attributed to the asymmetric and symmetric stretching vibration of the C–H bond [44]. The bands at 2880, 1690, and 1620 cm^{-1} were assigned to HCl [48], 2ν(C-Cl$_2$), and δ(H$_2$O) [45], respectively. There were bands at 1556, 1260, and 840-960 cm^{-1}, which were attributed to the vibration modes of ν(C=C), δ(CH-Cl), and ν(C-Cl) [48] in TCE. In addition, the band at 1050 cm^{-1} was recorded, which was attributed to the oxygen–oxygen stretching vibration of the chemisorbed oxygen species [26,49]. Intensity of the band assignable to the adsorbed oxygen species was much higher on 2.85AuPd$_{1.87}$/3DOM CeO$_2$ than that on 3DOM CeO$_2$, indicative of s more amount of the adsorbed oxygen species generated on the former sample. The band at 1465 cm^{-1} was ascribable to the carboxylate species [26,49] on the surface of the two samples, and its intensity was higher on 2.85AuPd$_{1.87}$/3DOM CeO$_2$ (Fig. 13A) than that on 3DOM CeO$_2$ (Fig. 13B), again confirming that AuPd$_{1.87}$ was the active site for TCE adsorption and TCE oxidation was more likely to occur at the interface between AuPd$_{1.87}$ alloy NPs and 3DOM CeO$_2$.

According to the results of the DRIFTS characterization and those reported previously, we propose that the oxidation of TCE over 2.85AuPd$_{1.87}$/3DOM CeO$_2$ might take place as follows:

$$CCl_2 = CHCl \xrightarrow[\text{M-Cl}]{Cl_2 or} CCl_3\text{-}CHCl_2 \xrightarrow{\text{-HCl}} CCl_2 = CCl_2 \qquad (1)$$

$$4HCl + O_2 \leftrightarrow 2Cl_2 + 2H_2O \qquad (2)$$

$$8CCl_2 = CHCl + 17O_2 \rightarrow 16CO_2 + 2H_2O + 10Cl_2 + 4HCl \qquad (3)$$

The C=C bond in TCE was activated and decomposed on the Lewis acid sites, followed by chlorination to form CCl$_3$CHCl$_2$. Then, the elimination of HCl took place with H abstraction by a basic O^{2-} species and dissociation of the C–Cl bond. It should be mentioned that a small amount of perchloroethylene (PCE) as a by-product was detected in the oxidation of TCE (Eq. (1)) over the 2.85AuPd$_{1.87}$/3DOM CeO$_2$ sample (Fig. S6). Similar phenomena were also observed by Feijen-Jeurissen et al. [39] and Gonzalez-Velasco et al. [50]. The gas-phase O$_2$ molecules were activated by picking up the electrons from 3DOM CeO$_2$ to form the O$_{ads}$ species, and the formed O$_{ads}$ species could activate the C–Cl and C=C bonds, hence promoting the oxidation of TCE. The loading of AuPd alloy NPs was also beneficial for generation of the O$_{ads}$ species, and the enhanced oxidation ability of the 2.85AuPd$_{1.87}$/3DOM CeO$_2$ sample could suppress the Cl addition of the C=C bond due to the fast C=C bond oxidation to CO$_2$. Generally speaking, the stronger the redox ability, the higher the Deacon reaction rate. The Deacon reaction (Eq.

(2)) gave rise to the release of the Cl species on the surface of the sample with redox ability. In addition, an electron transfer from AuPd to 3DOM CeO$_2$ was involved in the reaction mechanism. The active O$_{ads}$ species attacked the intermediates of TCE oxidation to form the oxygenate species and finally produce the products, such as CO$_2$, H$_2$O, HCl, and Cl$_2$ (Eq. (3)). The bimetallic Au–Pd NPs in 2.85AuPd$_{1.87}$/3DOM CeO$_2$ could enhance the reaction rate of TCE deep oxidation, thus reducing formation of the by-products.

4. Conclusions

3DOM CeO$_2$ was used as support to prepare Au–Pd alloy nanocatalysts via the PMMA-templating and PVA-protected reduction routes. All of the samples displayed a cubic fluorite-type crystal structure and a high-quality 3DOM architecture. The Au–Pd alloy NPs were well dispersed on the skeleton surface of 3DOM CeO$_2$. The 2.85AuPd$_{1.87}$/3DOM CeO$_2$ showed the highest catalytic activity ($T_{50\%}$ = 330 °C and $T_{90\%}$ = 415 °C at SV = 20,000 mL/(g h)), the highest TCE reaction rate at 300 °C (11.8 μmol/(g$_{Noble\ metal}$ s)), the highest TOF$_{Noble\ metal}$ at 300 °C (2.25×10^{-3} s^{-1}), the lowest activation energy (33 kJ/mol), the highest surface acidity, and good chlorine-tolerance in TCE oxidation, with tetrachloroethylene being the main by-product. Loading of the AuPd bimetallic alloys led to a change in reaction pathway and suppressed formation of perchloroethylene. It is concluded that well dispersed AuPd NPs, high O$_{ads}$ species concentration, good low-temperature reducibility, and strong interaction between AuPd alloy NPs and 3DOM CeO$_2$ as well as the distinctive 3DOM structure and high surface acidity were responsible for the good catalytic activity, stability, and chlorine-resistance of 2.85AuPd$_{1.87}$/3DOM CeO$_2$.

Acknowledgements

Appendix A. Supplementary data

Supplementary material related to this article can be found, in the online version, at doi:https://doi.org/10.1016/j.apcatb.2019.117879.

References

[1] E. Dobrzyńska, M. Pośniak, M. Szewczyńska, B. Buszewski, Crit. Rev. Anal. Chem. 40 (2010) 41–57.

[2] M.C. Wen, G.Y. Li, H.L. Liu, J.Y. Chen, T.C. An, H. Yamashita, Environ. Sci. Nano 6 (2019) 1006–1025.

[3] S.F. Zuo, P. Yang, X.Q. Wang, ACS Omega 2 (2017) 5179–15186.

[4] S. Pitkäaho, L. Matejova, S. Ojala, J. Gaalova, R.L. Keiski, Appl. Catal. B 111–114 (2012) 150–159.

[5] Q.Y. Chen, N. Li, M.F. Luo, J.Q. Lu, Catalytic oxidation of dichloromethane over Pt/ CeO$_2$−Al$_2$O$_3$ catalysts, Appl. Catal. B 127 (2012) 159–166.

[6] S.H. Xie, Y.X. Liu, J.G. Deng, S.M. Zang, Z.H. Zhang, H. Arandiyan, H.X. Dai, Environ. Sci. Technol. 51 (2017) 2271–2279.

[7] Y. Wang, H. Arandiyan, J. Scott, M. Akia, H.X. Dai, J.G. Deng, K.F. Aguey-Zinsou, R. Amal, ACS Catal. 6 (2016) 6935–6947.

[8] J.J. Kong, G.Y. Li, M.C. Wen, J.Y. Chen, H.L. Liu, T.C. An, J. Catal. 370 (2019) 88–96.

[9] P. Wei, D.D. Qin, J.Y. Chen, Y.X. Li, M.C. Wen, Y.M. Ji, G.Y. Li, T.C. An, Environ. Sci. Nano 6 (2019) 959–969.

[10] X. Yao, Z. Wang, S. Yu, F. Yang, L. Dong, Appl. Catal. A Gen. 542 (2017) 282–288.

[11] P. Yang, S.S. Yang, Z.N. Shi, Z.H. Meng, R.X. Zhou, Appl. Catal. B 162 (2015) 227–235.

[12] M. Sadakane, T. Horiuchi, N. Kato, C. Takahashi, W. Ueda, Chem. Mater. 19 (2007) 5779–5785.

[13] S.H. Xie, J.G. Deng, S.M. Zang, H.G. Yang, G.S. Guo, H. Arandiyan, H.X. Dai, J. Catal. 322 (2015) 38–48.

[14] H.N. Li, L. Zhang, H.X. Dai, H. He, Inorg. Chem. 48 (2009) 4421–4434.

[15] H. Zhang, L. Zhang, J.G. Deng, Y.X. Liu, H.Y. Jiang, F.J. Shi, K.M. Ji, H.X. Dai, Chin. J. Catal. 32 (2011) 842–852.

[16] P. Yang, X.M. Xue, Z.H. Meng, R.X. Zhou, Chem. Eng. J. 234 (2013) 203–210.

[17] Z. Li, L. Li, Q. Yuan, W. Feng, J. Xu, L. Sun, W. Song, C. Yan, J. Phys. Chem. C 112 (2008) 18405–18411.

[18] Y.M. Choi, H. Abernathy, H.T. Chen, M.C. Lin, M.L. Liu, ChemPhysChem 7 (2006) 1957–1963.

[19] L. Liu, Z. Yao, Y. Deng, F. Gao, B. Liu, L. Dong, ChemCatChem 3 (2011) 978–989.

[20] R. Si, Y.W. Zhang, S.J. Li, B.X. Lin, C.H. Yan, J. Phys. Chem. B 108 (2004) 12481–12488.

[21] P. Yang, Z.N. Shi, S.S. Yang, R.X. Zhou, Chem. Eng. Sci. 126 (2015) 361–369.

[22] H. Arandiyan, H.X. Dai, K.M. Ji, H.Y. Sun, J.H. Li, ACS Catal. 5 (2015) 1781–1793.

[23] Y. Liu, B.C. Liu, Q. Wang, C.Y. Li, W.T. Hu, Y.X. Liu, P. Jing, W.Z. Zhao, J. Zhang, J. Catal. 296 (2012) 65–76.

[24] S.H. Xie, J.G. Deng, Y.X. Liu, Z.H. Zhang, H.G. Yang, Y. Jiang, H. Arandiyan, H.X. Dai, C.T. Au, Appl. Catal. A Gen. 507 (2015) 82–90.

[25] Z.X. Wu, J.G. Deng, Y.X. Liu, S.H. Xie, Y. Jiang, X.T. Zhao, J. Yang, H. Arandiyan, G.S. Guo, H.X. Dai, J. Catal. 332 (2015) 13–24.

[26] S.H. Xie, Y.X. Liu, J.G. Deng, X.T. Zhao, J. Yang, K.F. Zhang, Z. Han, H.X. Dai, J. Catal. 342 (2016) 17–26.

[27] P. Hu, Y.F. Duan, W.K. Ding, J. Zhang, L.Y. Bai, N. Li, H.Q. Wei, Energy Fuels 31 (2017) 13852–13858.

[28] X.J. Yao, L. Zhang, L.L. Li, L.C. Liu, Y. Cao, X. Dong, F. Gao, Y. Deng, C.J. Tang, Z. Chen, L. Dong, Y. Chen, Appl. Catal. B 150–151 (2014) 315–329.

[29] S.H. Xie, J.G. Deng, Y.X. Liu, Z.H. Zhang, H.G. Yang, Y. Jiang, H. Arandiyan, H.X. Dai, C.T. Au, Appl. Catal. A Gen. 507 (2015) 82–90.

[30] H. Huang, Y.F. Gu, J. Zhao, X.Y. Wang, J. Catal. 326 (2015) 54–68.

[31] K.D. Chen, S.B. Xie, A.T. Bell, E. Iglesia, J. Catal. 198 (2001) 232–242.

[32] C. Li, K. Domen, K. Maruya, T. Onishi, J. Am. Chem. Soc. 111 (1989) 7683–7687.

[33] P. Steltenpohl, A. Aranzabal, R. López-Fonseca, J.I. Gutiérrez-Ortiz, J.R. González-Velasco, Catal. Today 62 (2000) 367–377.

[34] R. López-Fonseca, S. Cibrián, J.I. Gutiérrez-Ortiz, M.A. Gutiérrez-Ortiz, J.R. González-Velasco, AIChE J. 49 (2010) 496–504.

[35] P. Yang, S.F. Zuo, Z.N. Shi, F. Tao, R.X. Zhou, Appl. Catal. B 191 (2016) 53–61.

[36] Y.J. Bang, S.J. Han, J. Yoo, J.H. Choi, J.K. Lee, J.H. Song, J. Lee, I.K. Song, Appl. Catal. B 148–149 (2014) 269–280.

[37] Y.F. Gu, X.X. Jiang, W. Sun, S.X. Bai, Q.G. Dai, X.Y. Wang, ACS Omega 3 (2018) 8460–8470.

[38] B. Miranda, E. Díaz, S. Ordóñez, A. Vega, F.V. Díez, Appl. Catal. B 64 (2006) 262–271.

[39] M.M.R. Feijen-Jeurissen, J.J. Jornaa, B.E. Nieuwenhuysa, G. Sinquinb, Catal. Today 54 (1999) 65–79.

[40] J.I. Gutiérrez-Ortiz, R. López-Fonseca, U. Aurrekoetxea, J.R. González-Velasco, J. Catal. 218 (2003) 148–154.

[41] J. Wang, X.L. Liu, J.L. Zeng, T.Y. Zhu, Catal. Commun. 76 (2016) 13–18.

[42] T.T. Wang, Q.G. Dai, F.W. Yan, J. Chem. Eng. 34 (2017) 664–671.

[43] Q.G. Dai, S.X. Bai, X.Y. Wang, G.Z. Lu, Appl. Catal. B 129 (2013) 580–588.

[44] M. Trombetta, G. Busca, S.A. Rossini, V. Piccoli, U. Cornaro, J. Catal. 168 (1997) 334–348.

[45] J. Fan, J.T. Yates, J. Am. Chem. Soc. 118 (1996) 4686–4692.

[46] S.X. Bai, B.B. Shi, W. Deng, Q.G. Dai, X.Y. Wang, RSC Adv. 5 (2015) 48916–48927.

[47] L.A. Phillips, G.B. Raupp, J. Mol. Catal. 77 (1992) 297–311.

[48] J. Halasz, B. Imre, I. Hannus, Appl. Catal. A Gen. 271 (2004) 47–53.

[49] M. Schmal, M.V.M. Mariana, V.V. Souza, Monica Alegre, A.P.D. Silva, D.V. Cesar, C.A.C. Perez, Catal. Today 118 (2006) 392–401.

[50] A. Aranzabal, J.L. Ayastuy-Arizti, J.A. González-Marcos, J.R. González-Velasco, J. Catal. 214 (2003) 130–135.